Fuel 418 (2026) 138741

Contents lists available at ScienceDirect

Fuel

journal homepage: www.elsevier.com/locate/fuel

Full Length Article

Role of Transient-Plasma Generated Free Radicals in Hydrogen Combustion: Spectroscopic and Theoretical Insights

Curtis Hauck [a], Mariano Rubio [b], Fatemeh Afshar Ghahremani [c], Caleb Medchill [a], Fokion Egolfopoulos [b], Stephen B. Cronin [a,c,*]

[a] Ming Hsieh Department of Electrical Engineering, United States
[b] Department of Aerospace and Mechanical Engineering, United States
[c] Department of Chemistry, University of Southern California, Los Angeles, CA 90089, United States

ARTICLE INFO

Keywords:
Transient Plasma Ignition
Carbon Free Fuel
Hydrogen
In-situ Spectroscopy

ABSTRACT

Transient plasma ignition is known to improve the combustion of various fuels. Here, we compare the combustion mechanisms of carbon-free fuels containing mixtures of H_2 and O_2 via transient plasma ignition and conventional spark ignition. The transient plasma ignition is produced by five 20 ns pulses at a frequency of 1 kHz with an amplitude of 20 kV. Compared to conventional spark ignition (CSI), TPI ignited four times faster at a lean equivalence ratio ($\phi = 0.4$). Optical diagnostics confirmed the presence of H_α emission during TPI, providing direct evidence of atomic hydrogen radicals generated by nanosecond plasma discharges. These radicals, coupled with electrostatic flow effects, reduced ignition delay and accelerated flame propagation beyond enhancements attributable to flame wrinkling alone. Complementary kinetic modeling with Cantera and one-dimensional Lagrangian simulations revealed that plasma-generated H· radicals bypass high-temperature initiation pathways. This shortens induction times and promotes earlier OH· formation, thereby accelerating H_2 oxidation and water production under both adiabatic and non-adiabatic conditions. Together, these findings demonstrate that TPI enhances hydrogen combustion by coupling radical-driven kinetics with fluid-dynamic effects, offering a promising strategy to improve ignition reliability and efficiency in carbon-free propulsion systems.

1. Introduction

Recently, interest in the use of hydrogen as a fuel alternative has grown.[1,2] A drawback to hydrogen is its characteristic of being the lightest gas, resulting in low energy density per volume, and it is not naturally available on Earth.[3,4] However, hydrogen as a fuel has many benefits, including its high energy density per mass (120 $MJ \cdot kg^{-1}$) and its production of H_2O when combusting with O_2.[5] It is also considered to be a good fuel since it can combust under ultra-lean conditions, has high flame speeds, and has low ignition energies.[6] Hydrogen faces two primary challenges as a fuel: it is difficult to liquefy and thus transport, and its high flame temperature leads to significant NO_x formation through the Zeldovich mechanism. Recently, Zhang et al. demonstrated a strategy for hydrogen combustion in internal combustion engines by employing transient plasma–enhanced ignition of ultra-lean H_2 mixtures, which significantly reduced NOx emissions.[7] However, the underlying chemical and physical mechanisms of this enhancement are not well understood.

Although the enhancement mechanisms are generally poorly understood due to the complex relationship between plasma and flame kinetics, there has been success in the past in deriving plasma enhancement methods. Plane-to-plane dielectric barrier nanosecond pulsed discharges have shown increased kernel development.[8,9] Another study found nanosecond plasma-assisted combustion of CH_4 accelerated low-temperature fuel oxidation.[10] A study on short microwave pulse bursts was able to increase the flame speed by 25% and maintain combustion in ultra-lean conditions of CH_4 combustion with an equivalence ratio of 0.3.[11] Nagajara et al. found the effect of plasma chemistry was more effective in enhancing combustion during lean conditions.[12].

The nanosecond transient plasma is generated using a high-voltage nanosecond pulse system and operates with significantly lower energy consumption compared to conventional radio-frequency plasma sources.[13] Owing to its short-lived and non-equilibrium characteristics, the discharge constitutes a cold plasma—electron energies reach approximately 5 eV (corresponding to $\sim 10^4$ K), while the bulk gas and

* Corresponding author.
E-mail address: scronin@usc.edu (S.B. Cronin).

https://doi.org/10.1016/j.fuel.2026.138741
Received 4 December 2025; Received in revised form 30 December 2025; Accepted 8 February 2026
Available online 14 February 2026
0016-2361/© 2026 Elsevier Ltd. All rights are reserved, including those for text and data mining, AI training, and similar technologies.

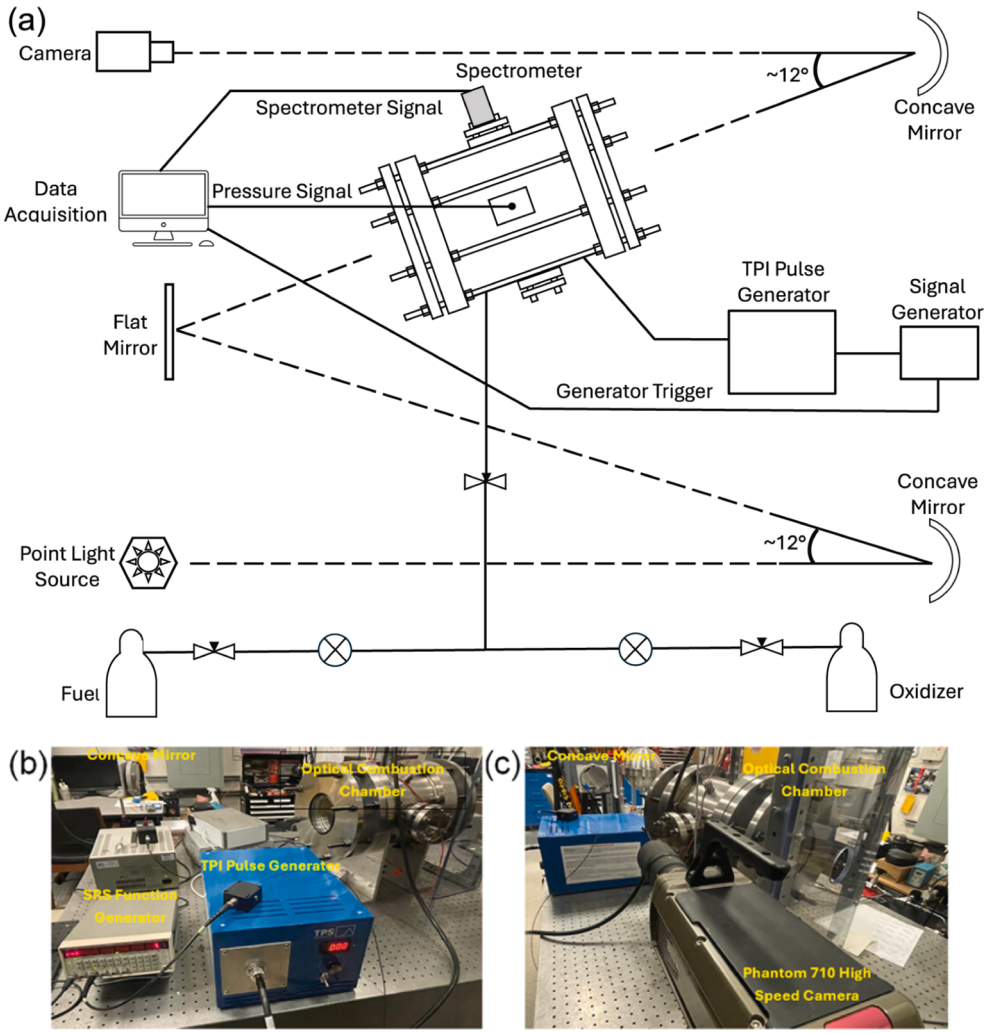


Fig. 1. (a) Diagram of the shadowgraph, optical emission spectrometer, and transient plasma systems, and (b, c) photographs of the combustion chamber with the transient plasma and shadowgraph systems.

molecular vibrational temperatures remain near ambient levels. These highly energetic electrons promote unique reaction pathways by forming transient intermediate species that cannot be achieved under thermal equilibrium conditions. The potential of nanosecond transient plasma systems has been widely demonstrated in applications such as nitric oxide (NO) remediation, an area that has been investigated for several decades using plasma-based techniques.[14–22].

Plasma-assisted combustion has received a lot of attention for its potential to extend flammability limits, increase efficiency and reliability, and ignite alternative fuels.[23,24] Although this paper does not aim to reproduce engine-relevant combustion conditions, it adopts a more canonical approach to isolate and examine the effects of transient plasma through the radicals formed during the earliest combustion time scales. This paper utilizes *in situ* optical spectroscopy, pressure–time traces, zero-dimensional chemical kinetics modeling, and one-dimensional Lagrangian simulations to investigate the mechanisms behind transient plasma-enhanced combustion.

2. Experimental methods

An investigation of radical formation and combustion characteristics is conducted in a cylindrical chamber composed of 316 stainless steel, featuring axial optical access for a shadowgraph system, as illustrated in Fig. 1. The chamber has a diameter of 27 cm and a length of 22 cm. It is capable of handling pressures up to 90 atm. Each end is capped with a fused quartz window, 15.2 cm in diameter and 7.6 cm thick. There is also a window in the center on the lateral side of the chamber to allow *in situ* optical emission spectroscopy. The windows are sealed to the chamber using heavy-duty O-rings. Two stainless steel electrodes are fitted perpendicular to the lateral wall. The electrodes are on opposite sides of the chamber, meet in front of the lateral window, and create a central ignition point.

A nanosecond pulse power supply was employed in this study. Pulse timing and synchronization were controlled using a Stanford Research Systems DG535 pulse generator, triggered via LabVIEW software, as viewed in Fig. 1. The resulting transient plasma represents a non-equilibrium, pulsed corona discharge.[25–27] This distributes energy over a broader volume than a conventional capacitive spark ignition (CSI) discharge and achieves higher electron energies.[25,26,28] These effects arise from efficient energy coupling between the applied electric fields and the fuel, facilitated by energetic electrons within the plasma.[27,28].

The conventional ignition system was derived from a General Motors high-energy ignition (HEI) configuration. It utilizes a 70:1 turn ratio, a 65 kV ignition coil, with triggering of the ignition module also controlled through LabVIEW software. Both the transient plasma discharge and CSI discharge voltages were monitored using a NorthStar PVM-1 (60 kV) probe, while the discharge current was recorded using a Pearson 110 current probe.

The voltage–time waveforms of the CSI discharge included a 3.5 kV

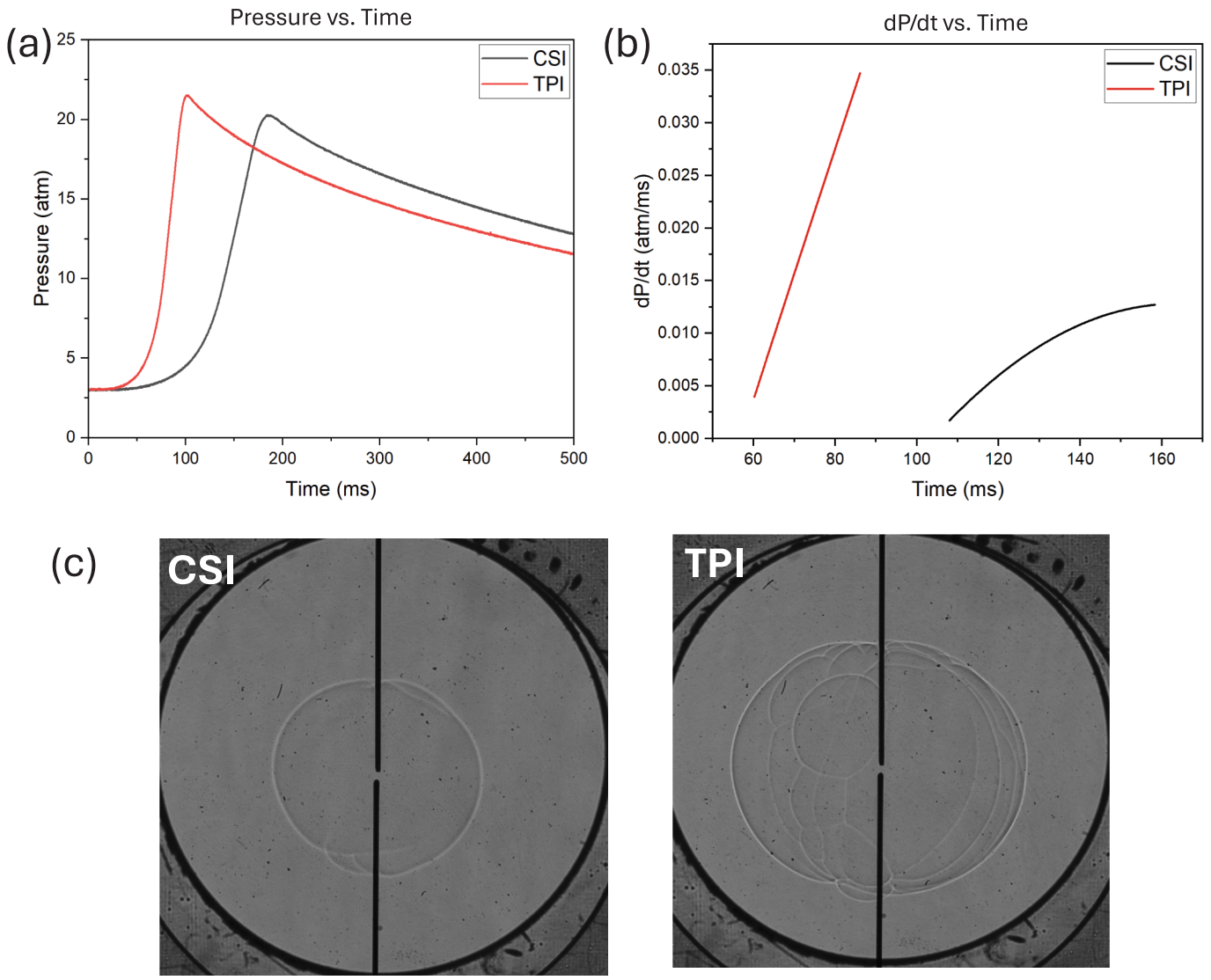


Fig. 2. Comparison of $0.4H_2 + 0.5O_2 + 3.0He$ combustion in a constant-volume combustion chamber at $\phi = 0.4$, $P_i = 3$ atm, and $T_i = 298$ K with (a) a plot showing pressure vs. time, (b) a plot showing the calculated rate of pressure change vs. time (dP/dt), and (c) images showing flame topology. Videos of these combustion events are provided in the Supplemental Material (SMV1 and SMV2).

peak voltage, 8 μs duration, and 56mJ energy output, as shown in Figure SMF1a. In contrast, the transient plasma ignition (TPI) discharge produced a 25 kV peak voltage, 20 ns pulse width at 2.5 kHz, and 18.6mJ energy, as seen in Figure SMF1b. The same discharge electrodes were used in both configurations; these were modified NGK D9EA copper-core spark plugs with the J-strap removed and stainless-steel center electrodes brazed in place to maintain a 1 mm gap between the discharge and return electrodes.

To image the flame propagation, a CMOS Phantom v710 high-speed camera capturing 25,000 frames per second was used for shadowgraph imaging with a 512x512 pixel window. A 601B1 Kistler dynamic pressure sensor was used in conjunction with a Kistler 5010B charge amplifier to send signals to a National Instruments 6259 DAQ analog input sampling at a rate of 100 kHz to record the pressure–time [*P, t*] trace during the experiment. The ignition signal trigger, the camera recording trigger, and the pressure recording trigger were synchronized and controlled using LabVIEW software. Chamber filling was accomplished by the partial pressure method with the use of Omega PX409-AV pressure transducers with the appropriate full-scale range to minimize uncertainties in the fuel/air equivalence ratio (ϕ).

The thermodynamic pressures increase due to the thermal expansion of gases during the exothermic combustion process, and are recorded in the constant-volume chamber. Initial combustion propagation and pressure changes have been studied extensively.[29–31] Figs. 2(a) and 3(a) depict the pressure vs. time traces obtained in the combustion chamber during the experiments. Figs. 2(b) and 3(b) show the plots of the pressure rise rates (dP/dt) calculated from the initial pressure rise during combustion. As seen in previous spherically expanding flame experiments, dP/dt is proportional to the burning rate, and is used in this analysis as an indicator of the overall reactivity to determine the trends of the effects of TPI and compare them to CSI in a qualitative form.[32,33] To minimize the effects of low Lewis (*Le*) numbers that may add to thermodiffusive instabilities typically seen in hydrogen combustion, helium (He) was used as the inert gas in place of nitrogen (N_2).

In situ optical emission spectroscopy was taken using an Ocean Optics USB 2000 + . This study used acquisition times of 25 ms and 50 ms for various fuel ratios. A UV-grade fused silica plano-convex lens with a relatively large collection angle for efficient light gathering was employed to collect light into the spectrometer. The collected spectra were analyzed using WiRE 3.3 software, with spectral features identified by reference to the NIST Basic Atomic Spectra Data Handbook and the Identification of Molecular Spectra (4th ed.) by R.W.B. Pearse and A.G.

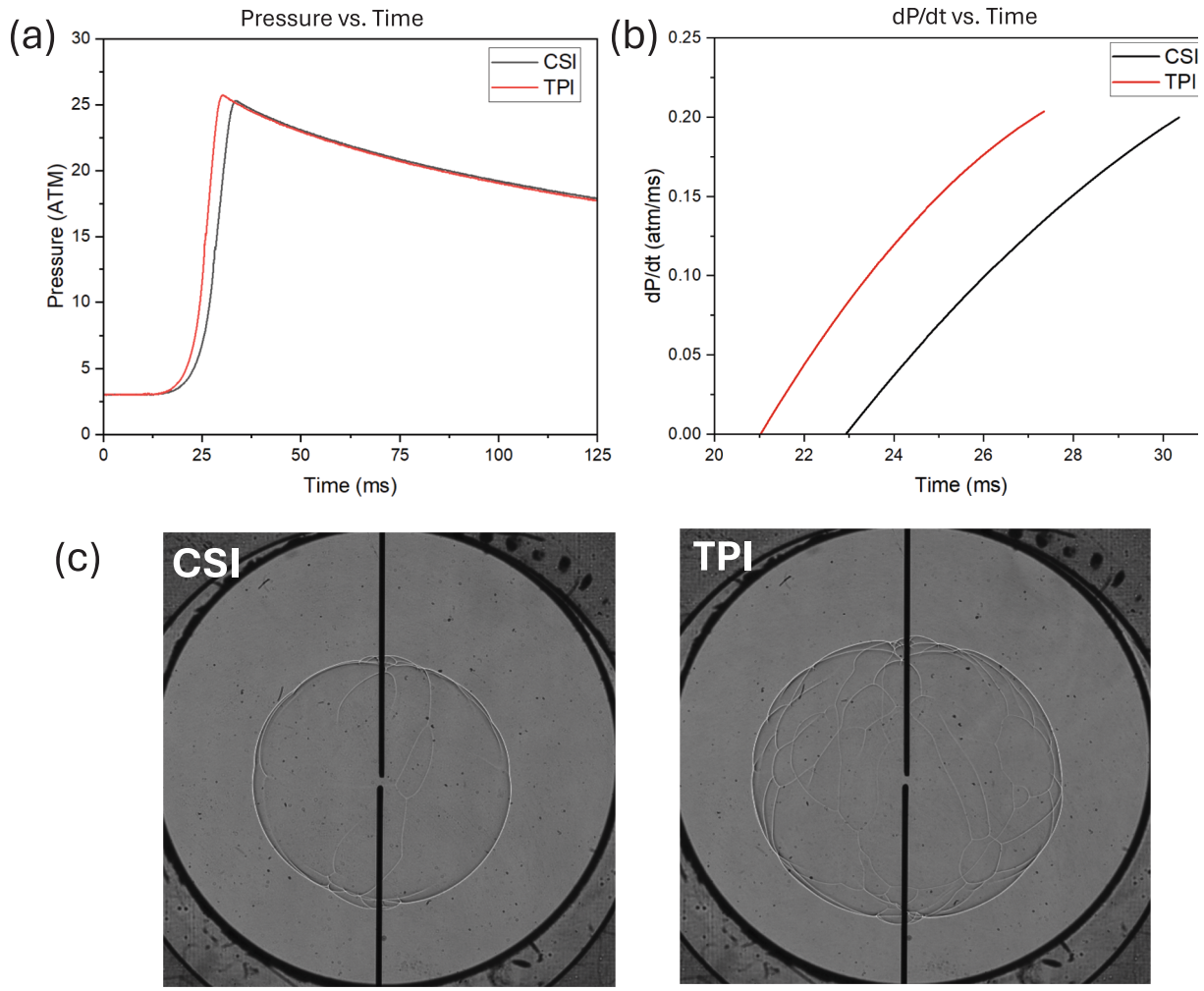


Fig. 3. Comparison of $0.6H_2 + 0.5O_2 + 3.0He$ combustion in a constant-volume combustion chamber at $\phi = 0.6$, $P_i = 3$ atm, and $T_i = 298$ K with (a) a plot showing pressure vs. time, (b) a plot showing the calculated rate of pressure change vs. time (dP/dt), and (c) images showing flame topology. Videos of these combustion events are provided in the Supplemental Material (SMV3 and SMV4).

Gaydon.[34,35].

3. Computational methods

The experiments were complemented by kinetic modeling using the Cantera suite and stable confined expanding flame modeling using a Lagrangian transient one-dimensional reacting flow code (LTORC).[36–38] This first-order modeling scheme enables us to perform a sensitivity analysis based on the intermediate species identified via spectroscopy and determine which chemical pathways dominate the combustion kinetics of H_2 under plasma discharge conditions (i.e., how the burn rate increases or decreases with the presence of various reactive radical species). It should be noted that the adopted initial H· injection does not aim to explicitly model the plasma discharge dynamics. Instead, it serves as an effective representation of the dominant chemical impact of plasma, namely the rapid generation of reactive hydrogen radicals, as evidenced by the measured H_α emission. Given the transient nature of the discharge and the strongly helium-diluted conditions, the plasma effect manifests primarily as an initial enhancement of the radical pool rather than as a sustained source term. This reduced-order approach enables isolation of the chemical role of plasma-generated radicals on combustion behavior while maintaining consistency with experimental observations. Here, we mimic the effect of the transient plasma in these calculations by introducing atomic H radicals (H·) in the initial reactant composition for two reasons. First, the H-H bond energy (~436 kJ/mol) is lower compared to O=O (~498 kJ/mole), and thus, H· is expected to be present in higher concentrations upon the transient plasma discharge compared to other radicals. Second, this estimate was confirmed by the plasma emission spectra shown in Figs. 4 and 5, which will be discussed below.

Given the multitude of simultaneous reaction pathways and the presence of transient radical species, it is essential to model the reactions and intermediates computationally to interpret the optical emission signatures captured during *in situ* spectroscopy throughout the ignition and combustion processes. We hypothesize that the dominant chemical pathways change in the presence of transient plasma discharge, leading to faster combustion rates.

The plasma-generated radicals are expected to short-circuit traditional reaction pathways, significantly accelerating oxidation and altering the flame structure and propagation characteristics. The modeling was carried out using a constant-pressure batch reactor model to decouple chemical kinetics from transport effects and to allow for the determination of the temporal distributions of temperature and species. The H_2 kinetic model used in the present study includes 57 species and 268 reactions.[39] Although this is a first-order modeling approach, it provides a practical and insightful framework for interpreting the experimental findings. Specifically, it will provide quantitative evidence of the positive effect of the plasma-generated radicals on the overall combustion process by bypassing slower, multi-step pathways and enabling more efficient energy release.

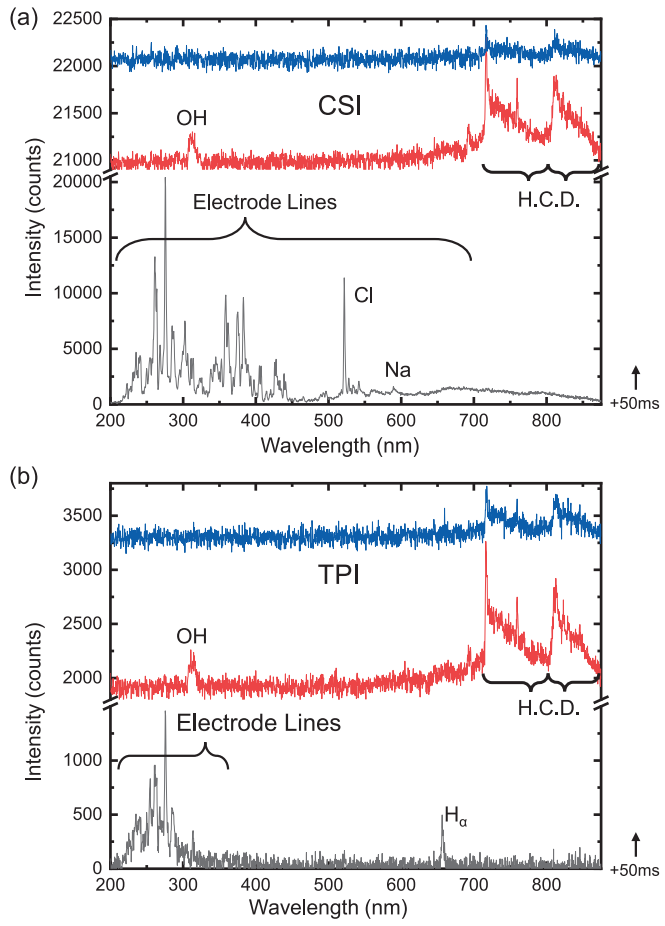


Fig. 4. Time-resolved plasma emission spectra taken with (a) conventional spark ignition and (b) transient plasma ignition of $H_2 + O_2 + He$ with a $\phi = 0.4$, a pressure of 3 atm, and $T_i = 298$ K.

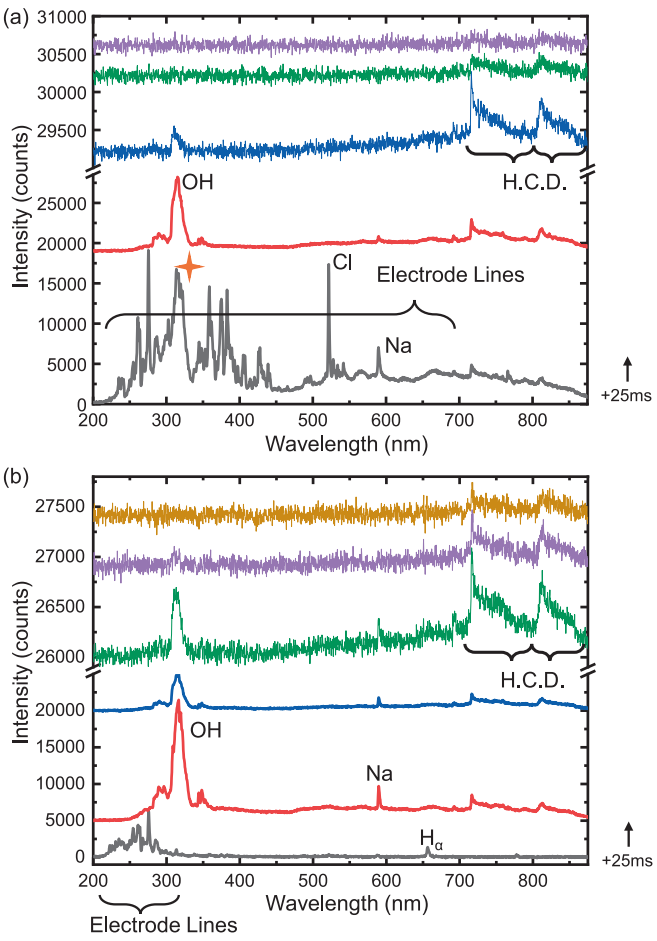


Fig. 5. Time-resolved plasma emission spectra taken with (a) conventional spark ignition and (b) transient plasma ignition of $H_2 + O_2 + He$ with a $\phi = 0.6$, a pressure of 3 atm, and $T_i = 298$ K.

To systematically investigate the role of plasma-generated H· radicals, we designed and implemented two distinct modeling scenarios using a constant-pressure batch reactor framework in Cantera. Scenario 1 was performed with energy exchange enabled (non-adiabatic/energy = on), allowing the reactor temperature to dynamically respond to the exothermicity of the H_2 oxidation reactions. This led to an increase in temperature accompanied by partial heat loss to the surrounding environment. Such conditions realistically simulate experimental setups where both radical-driven reaction acceleration and thermal feedback mechanisms influence combustion behavior. In this scenario, a fixed initial concentration of H· radicals was introduced at the start, with no continuous radical injection during the simulation. The evolution of radical concentrations was governed solely by the chemical kinetics described in the reaction network. The partial heat loss was modeled via an energy exchange term, preventing unlimited temperature rise and mimicking convective and conductive heat transfer present in practical reactors.

Scenario 2 was carried out with energy exchange disabled (adiabatic/energy = off), keeping the reactor temperature constant throughout the simulation. Here, heat produced by the chemical reactions did not affect the system temperature, effectively isolating the pure kinetic effects of the initially added H· radicals without thermal feedback. Like Scenario 1, only an initial fixed concentration of H· radicals were introduced, without any ongoing radical feed. This scenario serves as a thermal "control" case to decouple the effect of thermal acceleration from radical-driven kinetics, enabling a precise evaluation of non-thermal radical pathways.

The initial atomic hydrogen (H·) concentration was estimated based on the experimentally measured H_α line intensity obtained from transient plasma emission spectra of hydrogen combustion in $H_2/O_2/He$ mixtures. For an equivalence ratio of $\phi = 0.4$, the measured H_α intensity was approximately $I_{H_\alpha} \approx 500$, Fig. 4 while increasing the equivalence ratio to $\phi = 0.6$ resulted in an approximately twofold increase in the H_α intensity ($I_{H_\alpha} \approx 1000$, Figure 5).

Assuming a Boltzmann distribution for the excited-state populations and quasi-steady electron temperature conditions, the H_α emission intensity was taken to be proportional to the line-of-sight–integrated population of hydrogen atoms in the $n = 3$ excited state.[40] Under these assumptions, the inferred effective atomic hydrogen concentration corresponds to an upper-limit mole fraction of approximately 0.5% for both equivalence ratios.

The observed increase in H_α intensity with increasing equivalence ratio is attributed primarily to an expansion of the plasma-assisted reactive zone along the optical line of sight, rather than to a substantial change in the local atomic hydrogen mole fraction. Due to strong helium dilution, variations in the local total number density and gas composition with equivalence ratio remain limited. As a result, both the effective atomic hydrogen density and the effective total number density scale proportionally with the emitting length, leading to an approximately constant atomic hydrogen mole fraction across $\phi = 0.4$ and $\phi = 0.6$; the full calculation procedure is included in S1 of the Supplementary Material.

To assess the sensitivity of combustion behavior to uncertainties and spatial nonuniformities in radical production, the initial H· mole fraction was varied by factors of 0.5 and 0.25 relative to the nominal estimate

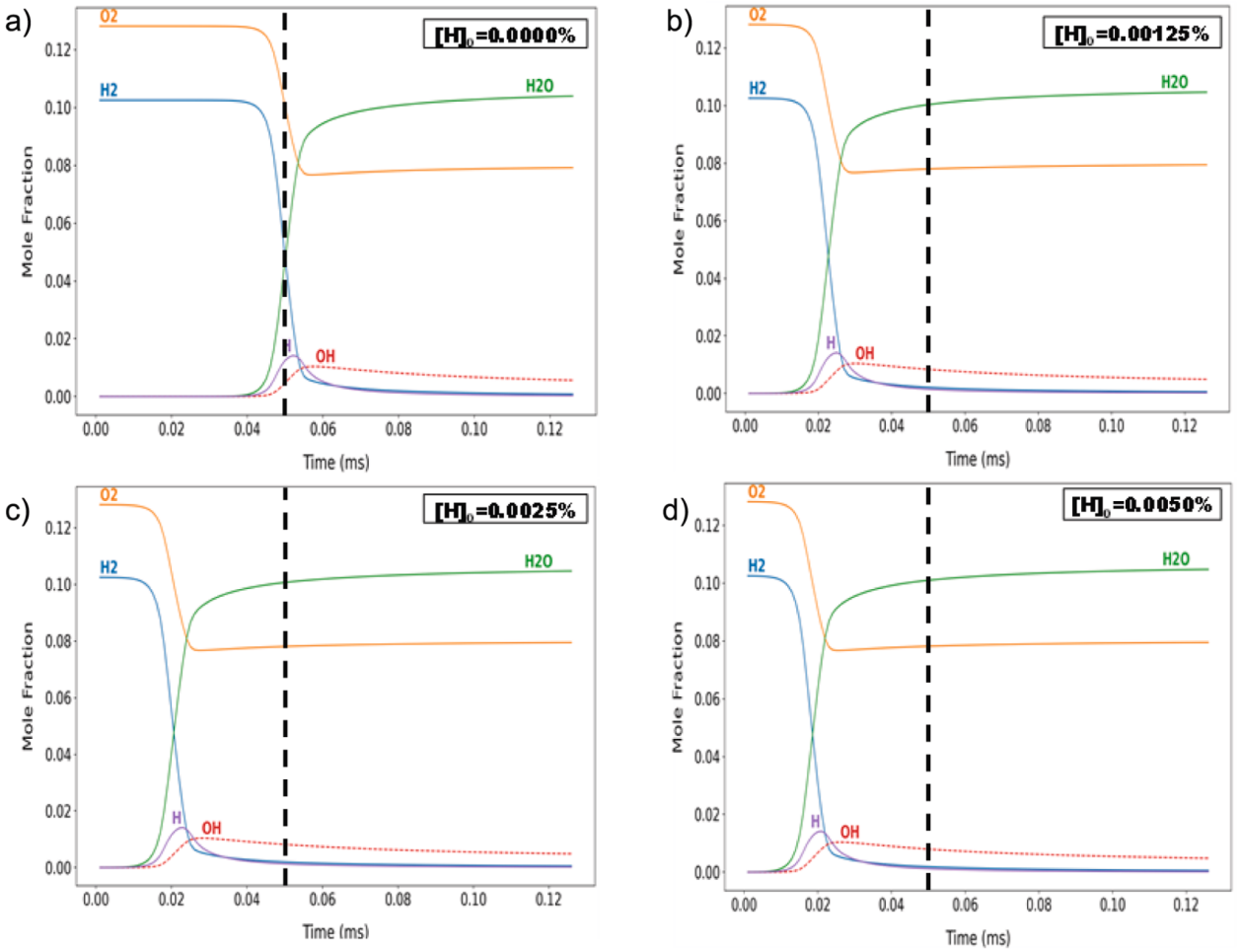


Fig. 6. Zero-dimensional kinetics modeling of $H_2 + O_2 + He$ ($f = 0.4$) combustion under varying concentrations of plasma-generated H· radicals, with external thermal energy on (non-adiabatic system). Rate of mole fraction change of H_2, O_2, H_2O, H, and OH vs. time ($P_0 = 3$ atm, $T_0 = 1100$ k, Mole Ratios: H_2: 0.4, O_2: 0.5, He: 3.0, H: H: (a) 0.0000%, (b) 0.00125%, (c) 0.0025%, and (d) 0.0050%, End-time:0.000125 s, time step: 1 μs).

(0.25% and 0.125%, respectively). This range spans a factor of four around the estimated value and captures plausible uncertainties in plasma-generated radical concentrations while maintaining physical consistency. The sensitivity analysis enables evaluation of the robustness of the observed combustion enhancement trends against variations in actual radical production. For both scenarios, the concentrations of other plasma-derived radicals (such as O, N, C, CN, C_2, OH, HO_2, CH, CH_2, CH_3, NO, and NH_2) were assumed to be constant to isolate and assess the specific impact of H· on the combustion dynamics.

The comparison of these two scenarios allows clear differentiation between the effects arising from radical chain branching and those due to thermal influences. This dual approach offers robust mechanistic insights into how plasma-generated radicals modulate H_2 combustion kinetics and clarifies how different thermal boundary conditions affect the time evolution of species concentrations and reaction rates.

Direct numerical simulation using LTORC was also carried out. By utilizing this one-dimensional simulation, the spatial relation between the kernel discharge areas of both TPI and CSI and the remaining quiescent mixture of the combustion chamber was modeled, and the reaction pathways were obtained and analyzed. As shown in Figs. 7 and 8, the model is initialized with two distinct areas: the area representing the ignition kernel area, which starts at 0 cm and extends to 0.3 cm, and the quiescent mixture area, which extends from 0.3 cm to 10 cm. In the kernel area, the TPI model keeps the discharge area at the same initial temperature as the rest of the mixture but includes an elevated amount of atomic H to simulate the formation of the H· typically formed by the non-thermal TPI discharge kernel. The CSI model was given an elevated temperature without any additional radicals in the kernel discharge area to simulate the thermal plasma of the CSI kernel. The amount of H· formed from the TPI discharge was calculated as a first-order analysis, based on the bond energy of the H-H bond (~436 kJ/mole) and estimating the percentage of hydrogen production in an $H_2 + O_2 + He$ environment at 298 K with five TPI plasma discharges adding 580mJ of energy. It was estimated that 30—50% of H_2 present in the ignition kernel area would be dissociated into atomic H. In both cases, 40% dissociated H_2 was used, where at a $\phi = 0.4$, the TPI kernel reactants were

$$0.24H_2 + 0.32H + 0.5O_2 + 3.0He$$

and at a $\phi = 0.6$, the kernel TPI reactants were

$$0.36H_2 + 0.48H + 0.5O_2 + 3.0He.$$

For the CSI simulation, the discharge area was left with the same reactants as the remainder of the chamber, with only temperature being elevated to simulate the spark discharge temperatures typically achieved in CSI discharge systems.[41]

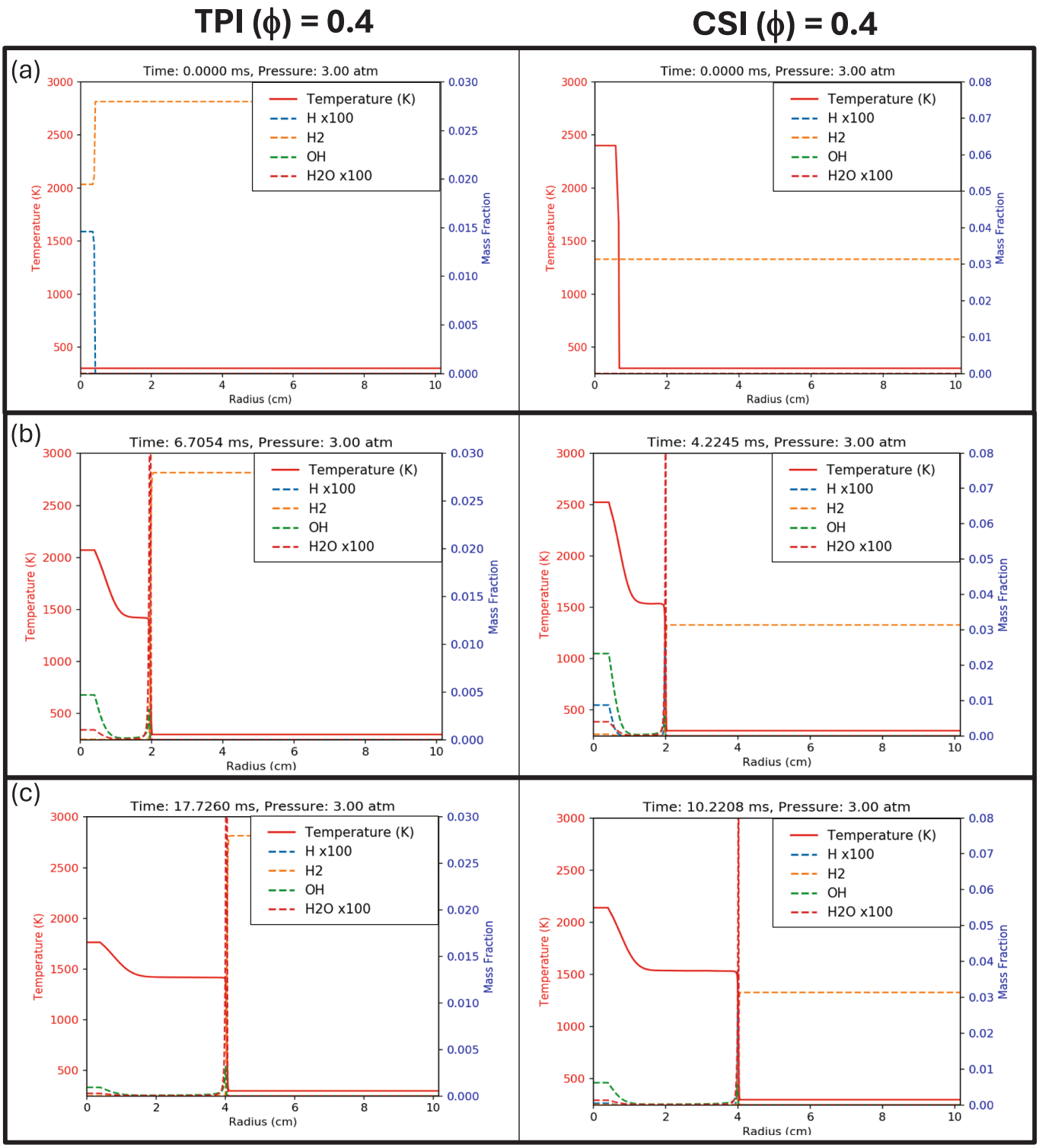


Fig. 7. One-dimensional simulation of $0.4H_2 + 0.5O_2 + 3.0He$ combustion at $\phi = 0.4$, $P_i = 3$ atm, and $T_i = 298$ K with (a) a comparison of the initial kernel conditions after TPI and CSI discharge, (b) the radical formation and temperature at a flame radius of 2 cm after ignition, and (c) the radical formation and temperature at a flame radius of 4 cm after ignition. Animations of the simulations are provided in the Supplemental Material (SMV5 and SMV6).

4. Results and Discussion

Fig. 2 shows the experimental results from the combustion of H_2 with O_2 and He at a $\phi = 0.4$, initial pressure (P_i) = 3 atm, and initial temperature (T_i) = 298 K. Fig. 2(a) shows the pressure vs time traces for both TPI and CSI-initiated combustion. To compare flame propagation speeds and determine the rate of pressure rise, a marker of pressures at 10% above P_i was used. At this pressure, it is seen that the TPI ignited mixture was over 200% faster than the CSI ignited mixture. Fig. 2(b) shows the corresponding dP/dt comparison, which relates to the flame propagation speed, and thus the burning rate, based on the Fiock and Marvin expression:

$$S_u = [dR_f/dP - (R_w^3 - R_f^3)/(3R_f^2\gamma_u)](dP/dt) = f(R_f, P)(dP/dt)$$

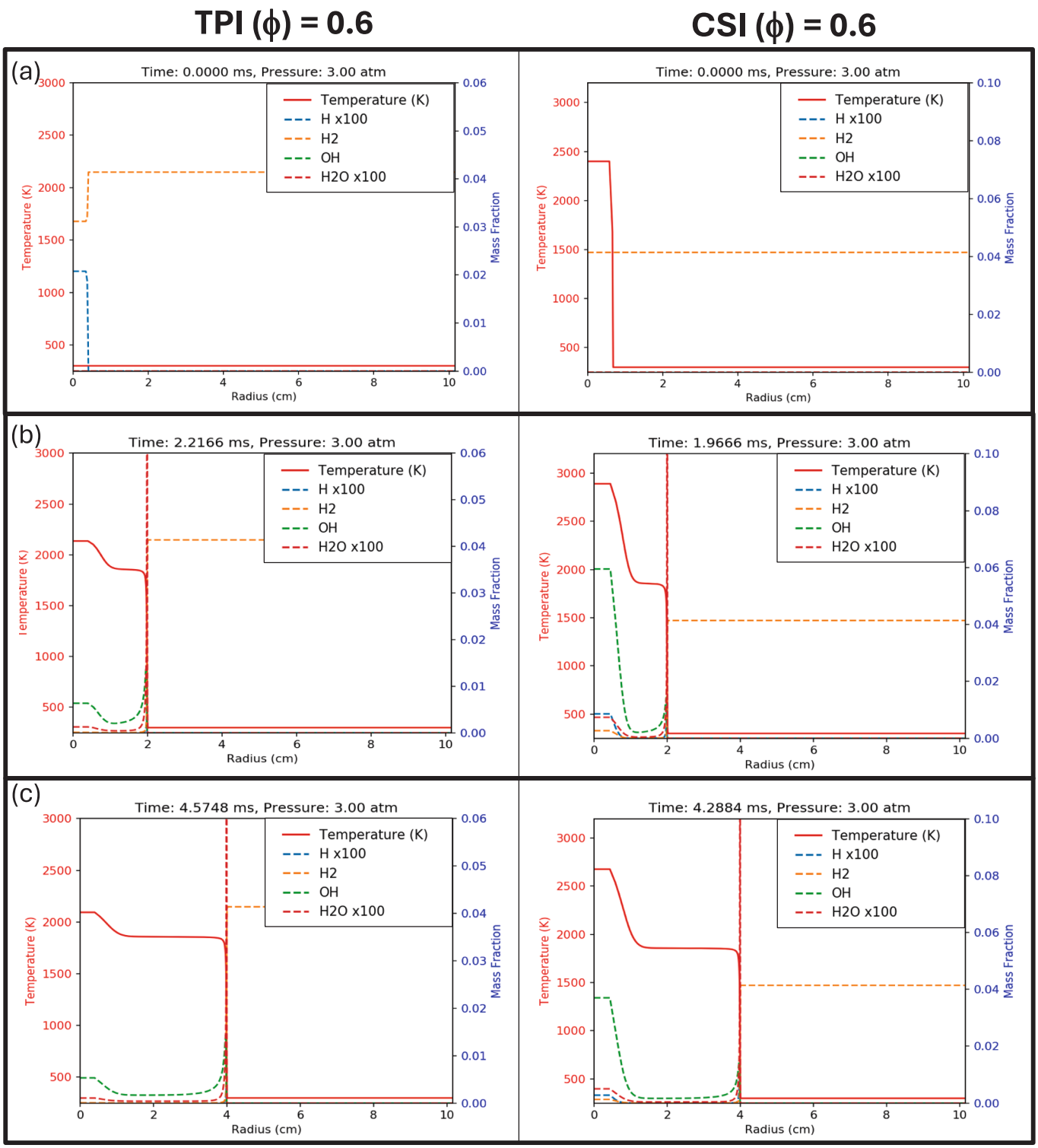


Fig. 8. One-dimensional simulation of $0.6H_2 + 0.5O_2 + 3.0He$ combustion at $\phi = 0.6$, $P_i = 3$ atm, and $T_i = 298$ K with (a) a comparison of the initial kernel conditions after TPI and CSI discharge, (b) the radical formation and temperature at a flame radius of 2 cm after ignition, and (c) the radical formation and temperature at a flame radius of 4 cm after ignition. Animations of the simulations are provided in the Supplemental Material (SMV7 and SMV8).

where R_w is the vessel radius, R_f is the flame's radius, P is the combustion pressure, and γ_u is the heat capacity ratio of the burning gas.[32,33] Fig. 2(c) shows images of the flames obtained by shadowgraph imaging. Here, the CSI ignited flame shows a relatively smooth flame front; the TPI ignited flame shows a greater amount of flame wrinkling, thereby creating a cellular structure. This wrinkling can be seen formed early on by the fluid motion created by the multi-discharge events of TPI when viewing the videos in the Supplemental Material (SMV2 and SMV4). Because of the increased surface area manifested by the flame wrinkling, an increased burning rate, as seen by the increase in the dP/dt plot of Fig. 2(b), is clearly apparent.

Fig. 3 shows the experimental results from the combustion of H_2 with O_2 and He at a $\phi = 0.6$, initial pressure (P_i) = 3 atm, and initial temperature (T_i) = 298 K. Fig. 3(a) shows the pressure vs time traces for both

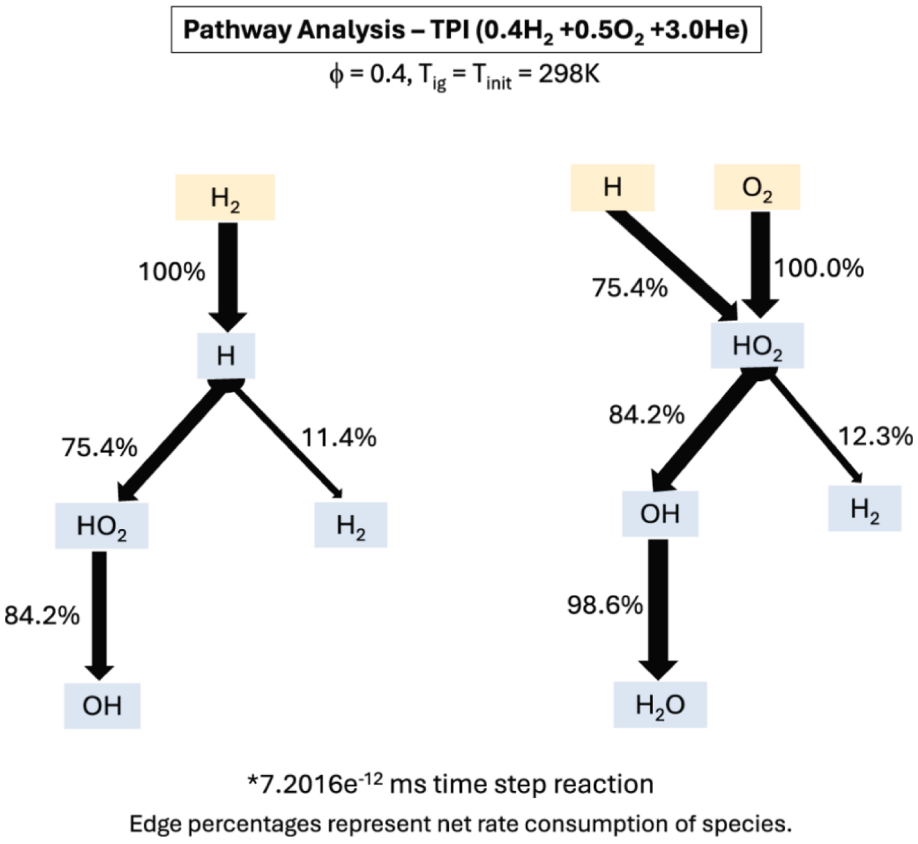


Fig. 9. Simplified reaction path diagram showing the consumption of H, H_2, and O_2 for the first time-step of the LTORC simulation of the $0.4H_2 + 0.5O_2 + 3.0He$ combustion directly proceeding the TPI discharge conditions. Reaction pathway tables are provided in the Supplemental Material (SMT1, SMT2, and SMT3).

TPI and CSI-initiated combustion. These results clearly show that the instabilities attributable to the flame wrinkling are present for both the TPI and CSI ignited flames. At a $\phi = 0.6$, the Lewis Number will be less than one, $Le_{\text{eff}} < 1$, and thermal-diffusive instabilities will now become a prominent characteristic of the flame. Even with the instabilities now present in the CSI combustion, TPI still ignites 12% faster than CSI. This suggests that another mechanism, such as the introduction of radicals, may be another advantage of the TPI ignition system.

Fig. 4 shows emission spectroscopy from CSI and TPI combustion of $H_2 + O_2 + He$ with a $\phi = 0.4$, a pressure of 3 atm, and $T_i = 298$ K. Fig. 4a displays the spectra from CSI ignition. Each spectrum was taken sequentially with 50 ms acquisition times. The initial spectra of the CSI combustion have plasma emission lines from the stainless-steel electrodes (labeled as electrode lines). These electrode lines were confirmed to be from the electrodes by collecting emission spectra of the CSI discharge in various gases individually. For example, spectra were taken in H_2, N_2, O_2, and He, and these spectra can be seen in Figure SMF3 in the Supplemental Material Document. In each spectrum, there was negligible variation compared to the features from H2 + O2 + He, verifying that the initial spectra in Fig. 4a are from the electrodes. Other notable features in the spectra containing CSI discharge (the black spectra in Fig. 4a) were Cl and Na lines. These are contamination lines, likely from a cleaner used on the quartz windows. The following spectra show the evolution of the flame (red and blue in Fig. 4a), dominated by peaks at 716 and 813 nm, each with tails extending into the infrared. Broad spectral features on the order of 100 nm are characteristic of vibrational–rotational transitions in hydrogen-containing diatomic species (H.C.D.).[34,42] The comparatively large rotational constants of these species, relative to diatomics such as CN, NO, or CO, give rise to the wider band structures observed.[43] As such, the structures between 716 nm and approximately 900 nm are attributed to H.C.D.s. The feature around 310 nm is characterized as OH.

Fig. 4b shows the TPI spectra of the flame of $H_2 + O_2 + He$ with a $\phi = 0.4$, a pressure of 3 atm, and $T_i = 298$ K. The plot shows sequentially taken spectra with 50 ms acquisition times. Similar to the CSI spectra, the initial spectra from the TPI discharge contain electrode lines. This was verified using the same technique as CSI. The spectra can be seen in Figure SMF2 in the Supplemental Material Document. Unique to TPI, a H_α peak from the hydrogen Balmer series is present in the discharge spectra. The red and blue spectra showing the evolution of the flame are again dominated by H.C.D.s and OH. The introduction of the H_α line is evidence of highly energetic radicals introduced into the system by the transient plasma.

The fuel used in Fig. 5 is $H_2 + O_2 + He$ with a $\phi = 0.6$, a pressure of 3 atm, and $T_i = 298$ K. Fig. 5a and 5b show sequential spectra (starting from the bottom) with acquisition times of 25 ms. The electrode lines from the spark discharge initially dominate the spectra from CSI ignition in Fig. 5a. The electrode lines were verified using the method described above. As with Fig. 4a, there are also Cl and Na contamination lines. However, new to this plot is the early development of the OH (orange star) and H.C.D. features beginning in the first 25 ms. Note the peak by the orange star is influenced by both OH and electrode lines, not one or

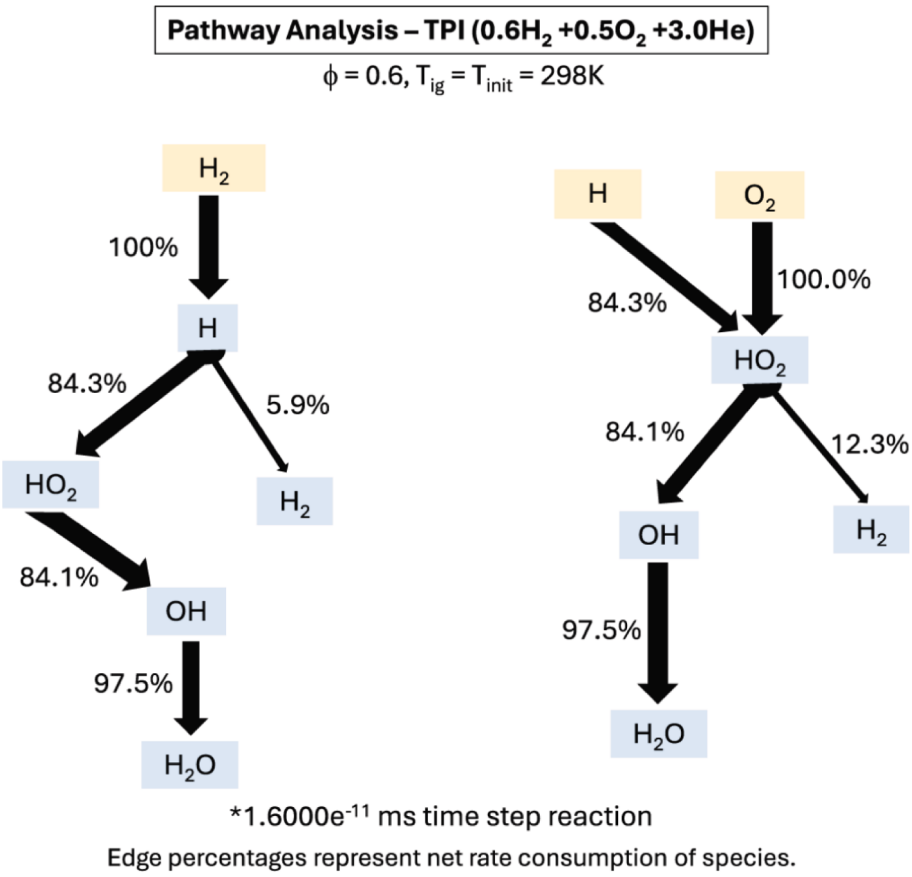


Fig. 10. Simplified reaction path diagram showing the consumption of H, H_2, and O_2 for the first time-step of the LTORC simulation of the $0.6H_2 + 0.5O_2 + 3.0He$ combustion directly proceeding the TPI discharge conditions. Reaction pathway tables are provided in the Supplemental Material (SMT4, SMT5 and SMT6).

the other. The following spectra are then dominated by H.C.D.s. For $H_2 + O_2 + He$ with a $\phi = 0.6$, the OH spectral feature is much more intense than the equivalence ratio at $\phi = 0.4$. This is true for both the CSI spectra (Fig. 5a) and the TPI spectra (Fig. 5b). The spectra containing the TPI discharge (the black spectrum in Fig. 5b) is again dominated by the electrode lines while also having the H_α line. The later spectra, which show the development of the flame, also exhibit Na contamination lines and the H.C.D. structures. The H_α peak is evidence of highly reactive radical species introduced into the flame kernel by the transient plasma discharge.

Fig. 6 shows the modeling results for lean $H_2 + O_2 + He$ non-adiabatic combustion at $\phi = 0.4$ (Energy is On, indicating the system is non-adiabatic), representing scenario 1. Additionally, the influence of plasma-generated neutral H· radicals on $H_2 + O_2 + He$ combustion was systematically investigated by varying their initial concentrations under otherwise identical conditions (T = 1100 K). The results show that the addition of H· generated by plasma plays a pivotal role in accelerating and optimizing the oxidation reactions of $H_2 + O_2 + He$. In the absence of these radicals, the initiation of combustion heavily relies on the thermal cleavage of H_2's H–H bonds, which, due to their relatively high activation energy (~436 kJ/mol), proceeds intrinsically slowly. This means the system requires either very high temperatures or prolonged residence times to achieve acceptable reaction rates. The plasma discharge introduces H· radicals, effectively bypassing the conventional high-temperature ignition pathway.

Figs. 7 and 8 show the spatial relationship of the formation of radicals for CSI and TPI, allowing for an investigation into the reaction pathway analysis of each fuel implementation at early timesteps of flame propagation. The simplified pathway analysis in Figs. 9 and 10 of the early time steps for the LTORC simulation shows that a recombination of H· to form H_2 presents a distinct source for the thermal energy needed for combustion.[44] Higher H· levels result in a more rapid rise of OH·, which further amplifies the oxidation pathways of H_2, as indicated by the time-resolved concentration plots (Figs. 6 and 11) and the Lagrangian combustion simulations in Figs. 7 and 8. This can again be attributed to both the recombination of H· to form H_2 and H with O_2 to produce both HO_2· and OH· earlier in the flame propagation. Furthermore, the data indicates that increasing the initial H· concentration—through stronger plasma discharge or parameter adjustments—reduces induction time and accelerates the formation of stable products such as H_2O. As seen in Figs. 12 and 13, CSI-ignited combustion simplified reaction pathway analysis from the LTORC simulation shows the dependency of the reaction of H_2 with O_2 during the early time steps of combustion, which then produces the typical oxidation pathways to form OH· and HO_2·. It can be noted that little recombination of H at elevated temperatures is observed.

From a practical standpoint, these findings are highly significant, as they indicate that employing plasma as a source of H· radicals can stabilize and efficiently promote H_2 combustion even under lean conditions, which are inherently challenging. In other words, plasma supplies pre-formed radicals that lessen the need for high initial thermal energy, providing an effective strategy to reduce temperature or pressure requirements in combustion systems. Figure SMF4 in the Supplemental Material shows the modeling results for lean $H_2 + O_2 + He$ adiabatic

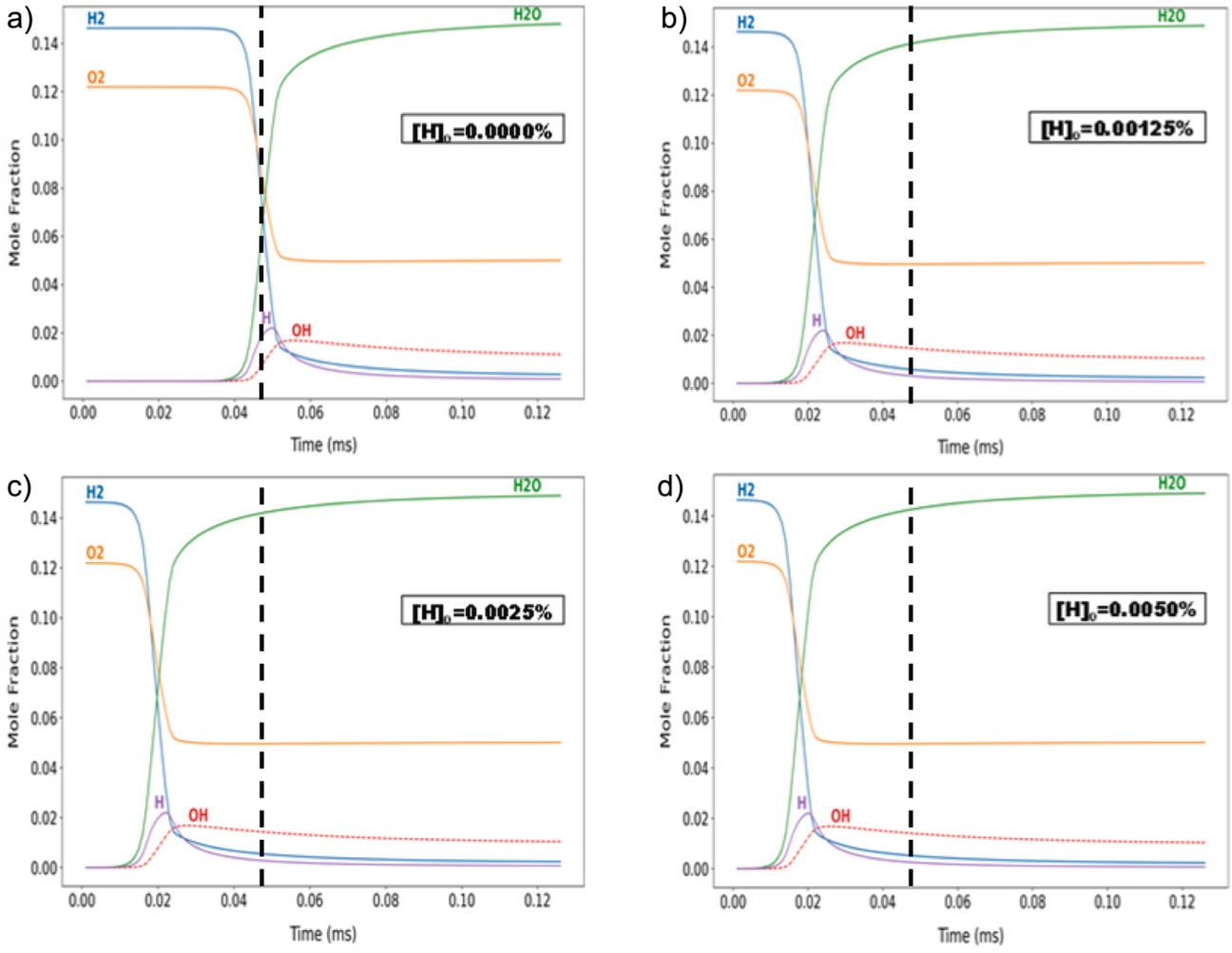


Fig. 11. Zero-dimensional kinetics modeling of $H_2 + O_2 + He$ ($\phi = 0.6$) combustion under varying concentrations of plasma-generated H· radicals, with external thermal energy on (non-adiabatic system). Rate of mole fraction change of H_2, O_2, H_2O, H, & OH vs. time ($P_0 = 3$ atm, $T_0 = 1100$ k, Mole Ratios: H_2: 0.6, O_2: 0.5, He: 3.0, H: H: (a) 0.0000%, (b) 0.00125%, (c) 0.0025%, & (d) 0.0050%, End-time:0.000125 s, time step: 1 μs).

combustion at $\phi = 0.4$ (Energy is Off, which means the system is adiabatic), representing Scenario 2. A comparative analysis of the simulation results under two key scenarios—Energy-On (adiabatic with thermal input) and Energy-Off (non-adiabatic without external heating but with injected H· radicals)—clearly demonstrates that the presence of neutral H· plays a pivotal role in accelerating H_2 combustion, independent of mere thermal effects.

In the Energy-Off case, where no additional thermal energy is supplied to the system, the introduction of H· alone significantly reduces the ignition delay time and leads to an earlier and more pronounced rise in OH· concentrations. These OH· peaks, clearly visible in the plots, serve as direct indicators of the onset and propagation of oxidation chain reactions. OH· acts as a highly effective chain carrier, reacting readily with H_2 to form more H·, thus rapidly driving the system toward the formation of H_2 and H_2O, as shown in Fig. 14.

In the Energy-On case at an initial temperature of 1100 K, the addition of H· accelerates H_2 consumption and shifts the onset of OH· peaks to much earlier times, even with direct thermal energy present. This indicates that plasma-generated species (such as H·) engage in non-adiabatic radical pathways that bypass conventional multi-step thermal mechanisms and lower activation barriers. Across both Energy-On and Energy-Off conditions, the consistent early appearance of OH· peaks at elevated temperatures provides strong evidence that the combustion acceleration cannot be explained by temperature effects alone. Rather, a substantial portion arises from non-thermal radical processes initiated by plasma species, which significantly enhance H_2 combustion beyond purely thermal effects alone.

Also, when ϕ increases from 0.4 to 0.6 (Figure SMF4 and Figure SMF5), we observe similar results in both the ignition delay and the mechanism modifications induced by the plasma-generated hydrogen atoms. This can be considered a strong indication that varying the H_2 concentration or reducing O_2, as the oxidizer, does not lead to significant changes, and the flame can therefore remain stable.

5. Conclusion

This study demonstrates that transient plasma ignition (TPI) significantly enhances hydrogen combustion by decreasing the ignition

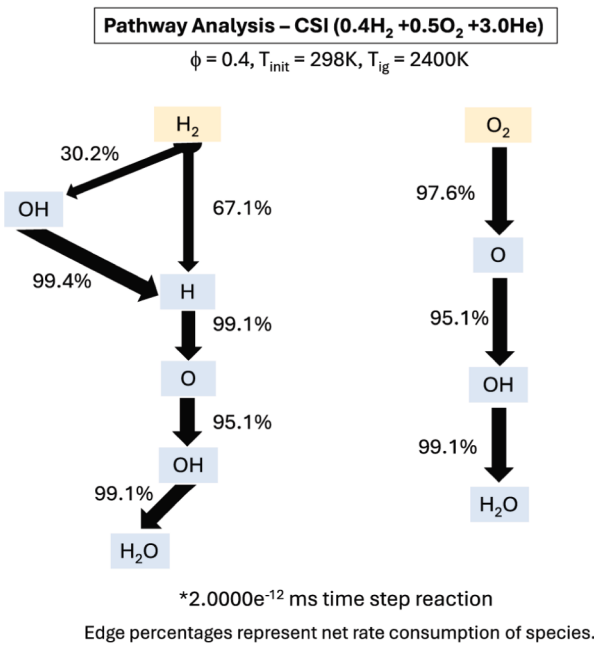


Fig. 12. Simplified reaction path diagram showing the consumption of H_2 and O_2 for the first time-step of the LTORC simulation of the $0.4H_2 + 0.5O_2 + 3.0He$ combustion directly proceeding the CSI discharge conditions. Reaction pathway tables are provided in the Supplemental Material (SMT7 and SMT8).

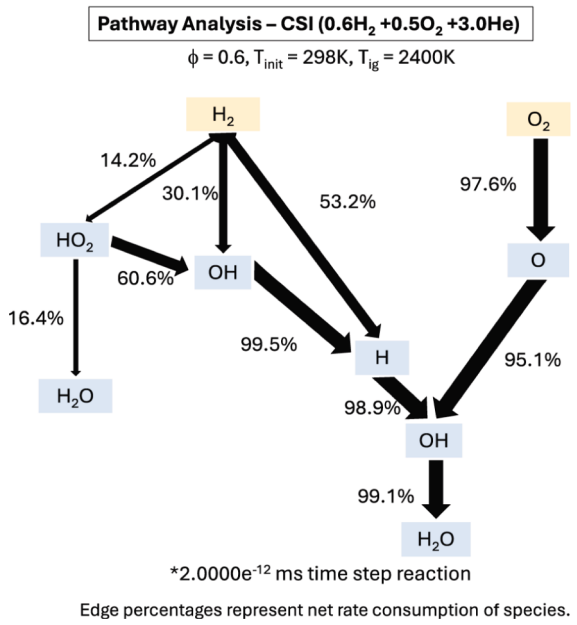


Fig. 13. Simplified reaction path diagram showing the consumption of H_2 and O_2 for the first time-step of the LTORC simulation of the $0.6H_2 + 0.5O_2 + 3.0He$ combustion directly proceeding the CSI discharge conditions. Reaction pathway tables are provided in the Supplemental Material (SMT9 and SMT10).

threshold in lean mixtures and accelerating flame propagation compared to conventional spark ignition (CSI). Constant-volume combustion experiments revealed more than a twofold decrease in the initial time for pressure to rise and up to a fourfold increase in the pressure rate (dP/dt) when transient plasma ignition was applied. These enhancements were observed at both $\phi = 0.4$ and $\phi = 0.6$, despite the CSI flame fronts developing instabilities as well at $\phi = 0.6$. Thus, the improvements cannot be explained solely by flame wrinkling, but from both physical and chemical effects. Nanosecond high-voltage pulses generate electrostatic forces that promote fluid motion and multi-scale mixing, while rapid discharge produces atomic hydrogen radicals that reduce ignition delay and increase burn rates. Optical emission spectroscopy confirmed the presence of H· radicals via the presence of H_α lines during TPI ignition. Zero-dimensional chemical kinetics modeling confirms the role of hydrogen radicals in driving faster combustion, and one-dimensional Lagrangian simulations identify the radical formation pathways under plasma-assisted versus conventional ignition conditions. Plasma-generated H· radicals bypass high-temperature ignition pathways, decreasing induction time and accelerating H_2O formation—conditions that would otherwise require prolonged residence times or very high thermal energies under CSI. Overall, transient plasma ignition offers a promising route to improve the performance of carbon-free hydrogen combustion by coupling radical chemistry with enhanced flow dynamics.

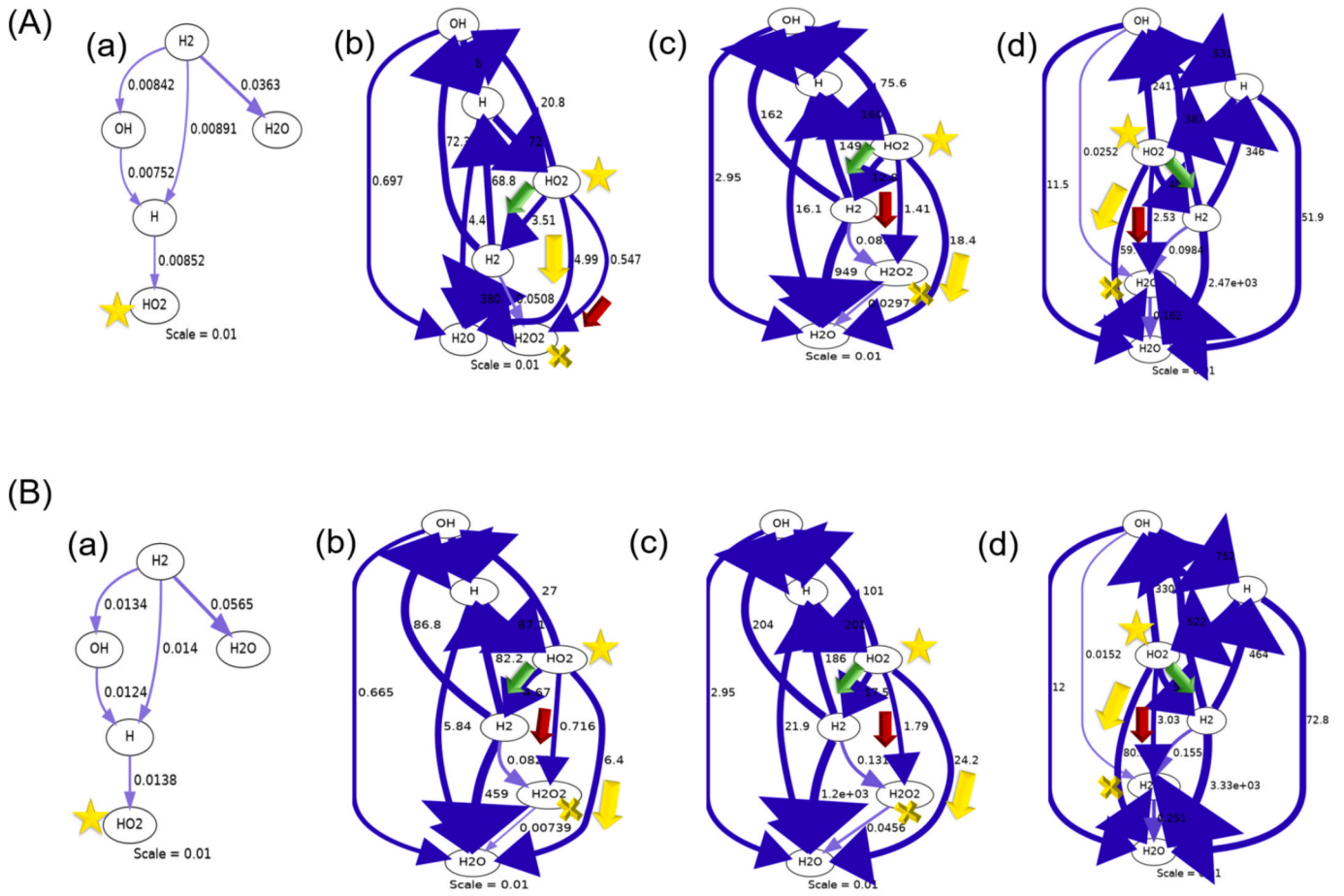


Fig. 14. Reaction path diagram for hydrogen radical (H·) for $H_2 + O_2 + He$ combustion under varying concentration of plasma-generated H·. A) $\phi = 0.4$, B) and $\phi = 0.6$, ($P_0 = 3$ atm, $T_0 = 1100$ k, Mole Ratios: H_2: 0.4/0.6, O_2: 0.5, He: 3.0, H: H: (a) 0.0000%, (b) 0.00125%, (c) 0.0025%, & (d) 0.0050%, End-time:0.000125 s, time step: 1e-5). The bold blue lines represent the main reaction paths. (For interpretation of the references to colour in this figure legend, the reader is referred to the web version of this article.)

CRediT authorship contribution statement

Curtis Hauck: Writing – review & editing, Writing – original draft, Validation, Methodology, Investigation, Formal analysis, Data curation. **Mariano Rubio:** Writing – original draft, Validation, Software, Methodology, Investigation, Formal analysis, Data curation. **Fatemeh Afshar Ghahremani:** Writing – original draft, Software, Formal analysis. **Caleb Medchill:** Writing – original draft, Conceptualization. **Fokion Egolfopoulos:** Supervision, Resources, Conceptualization. **Stephen B. Cronin:** Writing – review & editing, Writing – original draft, Supervision, Resources, Project administration, Funding acquisition, Conceptualization.

Declaration of competing interest

The authors declare that they have no known competing financial interests or personal relationships that could have appeared to influence the work reported in this paper.

Acknowledgements

This research was supported by the Army Research Office (ARO) Award No. W911NF2210284 (C.H.), the Air Force Office of Sponsored Research (AFOSR) award No. FA9550-24-1-0050 (C.M.), the National Science Foundation (NSF) Award no CBET-252974 (F.A.G.), and the USC Ershaghi Center on Energy Transition (E-CET) (M.R.).

Appendix A. Supplementary data

Supplementary data to this article can be found online at https://doi.org/10.1016/j.fuel.2026.138741.

Data availability

Data will be made available on request.

References

[1] Falcone PM, Hiete M, Sapio A. Hydrogen economy and sustainable development goals: Review and policy insights. Curr Opin Green Sustainable Chem 2021;31:100506.
[2] Liu Z, Kendall K, Yan X. China progress on renewable energy vehicles: fuel cells, hydrogen and battery hybrid vehicles. Energies 2018;12:54.
[3] Yue M, Lambert H, Pahon E, Roche R, Jemei S, Hissel D. Hydrogen energy systems: a critical review of technologies, applications, trends and challenges. Renew Sustain Energy Rev 2021;146:111180.
[4] Hu G, Chen C, Lu HT, Wu Y, Liu C, Tao L, et al. A review of technical advances, barriers, and solutions in the power to hydrogen (P2H) roadmap. Engineering 2020;6:1364–80.
[5] Guilbert D, Vitale G. Hydrogen as a Clean and Sustainable Energy Vector for Global transition from Fossil-based to Zero-Carbon. Clean Technol 2021;3:881–909.
[6] Kumar V, Gupta D, Kumar N. Hydrogen use in internal combustion engine: a review. International Journal of Advanced Culture Technology 2015;3:87–99.
[7] Zhang B, Rubio M, Tobar Lam JE, Ortiz-Ramirez A, Riggs T, Hernandez O, et al. Transient plasma enhanced combustion of ultra-lean H2 in an internal combustion engine for reduced NOx emission. Fuel 2025;381:133233.
[8] Yin Z, Adamovich IV, Lempert WR. OH radical and temperature measurements during ignition of H2-air mixtures excited by a repetitively pulsed nanosecond discharge. Proc Combust Inst 2013;34:3249–58.

[9] Nagaraja S, Yang V, Yin Z, Adamovich I. Ignition of hydrogen–air mixtures using pulsed nanosecond dielectric barrier plasma discharges in plane-to-plane geometry. Combust Flame 2014;161:1026–37.
[10] Sun W, Won SH, Ombrello T, Carter C, Ju Y. Direct ignition and S-curve transition by in situ nano-second pulsed discharge in methane/oxygen/helium counterflow flame. Proc Combust Inst 2013;34:847–55.
[11] Michael JB, Chng TL, Miles RB. Sustained propagation of ultra-lean methane/air flames with pulsed microwave energy deposition. Combust Flame 2013;160:796–807.
[12] Nagaraja S, Li T, Sutton JA, Adamovich IV, Yang V. Nanosecond plasma enhanced H2/O2/N2 premixed flat flames. Proc Combust Inst 2015;35:3471–8.
[13] Tsang W, Hampson R. Chemical kinetic data base for combustion chemistry. Part I. methane and related compounds. J Phys Chem Ref Data 1986;15:1087–279.
[14] Harding LB, Klippenstein SJ, Georgievskii Y. Reactions of oxygen atoms with hydrocarbon radicals: a priori kinetic predictions for the CH3+ O, C2H5+ O, and C2H3+ O reactions. Proc Combust Inst 2005;30:985–93.
[15] Hong Z, Davidson DF, Barbour EA, Hanson RK. A new shock tube study of the H+ O2→ OH+ O reaction rate using tunable diode laser absorption of H2O near 2.5 μm. Proc Combust Inst 2011;33:309–16.
[16] Huang M-B, Chen B-Z, Wang Z-X. Theoretical study of CH+ O2 reactions. Chem A Eur J 2002;106:5490–7.
[17] Irdam EA, Kiefer JH, Harding LB, Wagner AF. The formaldehyde decomposition chain mechanism. Int J Chem Kinet 1993;25:285–303.
[18] Jasper AW, Klippenstein SJ, Harding LB, Ruscic B. Kinetics of the reaction of methyl radical with hydroxyl radical and methanol decomposition. Chem A Eur J 2007;111:3932–50.
[19] Johnson MV, Goldsborough SS, Serinyel Z, O'Toole P, Larkin E, O'Malley G, et al. A shock tube study of n-and iso-propanol ignition. Energy Fuel 2009;23:5886–98.
[20] Joshi AV, Wang H. Master equation modeling of wide range temperature and pressure dependence of CO+ OH→ products. Int J Chem Kinet 2006;38:57–73.
[21] Kim K, Michael J. The thermal reactions of CH3. Symposium (International) on Combustion, Elsevier 1994:713–9.
[22] Klippenstein SJ, Miller JA, Harding LB. Resolving the mystery of prompt CO2: the HCCO+ O2 reaction. Proc Combust Inst 2002;29:1209–17.
[23] Starikovskaia SM. Plasma assisted ignition and combustion. J Phys D Appl Phys 2006;39:R265.
[24] Starikovskii AY. Plasma supported combustion. Proc Combust Inst 2005;30:2405–17.
[25] Jianbang L, Fei W, Guoqiang L, Kuthi A, Gutmark EJ, Ronney PD, et al. Transient plasma ignition. IEEE Trans Plasma Sci 2005;33:326–7.
[26] J.-b. Liu, P.D. Ronney, M.A. Gundersen, Premixed flame ignition by transient plasma discharges, 2002.
[27] Shukla B, Gururajan V, Eisazadeh-Far K, Windom BC, Singleton DR, Gundersen MA, et al. Effects of electrode geometry on transient plasma induced ignition. J Phys D Appl Phys 2013;46.
[28] Singleton DR, Gundersen MA. Transient Plasma Fuel–Air Ignition. IEEE Trans Plasma Sci 2011;39:2214–5.
[29] Xiouris C, Ye T, Jayachandran J, Egolfopoulos FN. Laminar flame speeds under engine-relevant conditions: uncertainty quantification and minimization in spherically expanding flame experiments. Combust Flame 2016;163:270–83.
[30] Lewis B, Von Elbe G. Determination of the speed of flames and the temperature distribution in a spherical bomb from time-pressure explosion records. J Chem Phys 1934;2:283–90.
[31] Movaghar A, Lawson R, Egolfopoulos FN. Confined spherically expanding flame method for measuring laminar flame speeds: Revisiting the assumptions and application to C1C4 hydrocarbon flames. Combust Flame 2020;212:79–92.
[32] Tian Z, Li Y, Zhang L, Glarborg P, Qi F. An experimental and kinetic modeling study of premixed NH3/CH4/O2/Ar flames at low pressure. Combust Flame 2009;156:1413–26.
[33] Varea E, Modica V, Vandel A, Renou B. Measurement of laminar burning velocity and Markstein length relative to fresh gases using a new postprocessing procedure: Application to laminar spherical flames for methane, ethanol and isooctane/air mixtures. Combust Flame 2012;159:577–90.
[34] Shull H, Pearse RWB, Gaydon AG. the identification of molecular spectra. Spectrochim Acta 1951;4:427.
[35] A.a.R. Kramida, Yu. and Reader, J. and NIST ASD Team, NIST Basic Atomic Spectra Data Handbook, National Institute of Standards and Technology, 2023.
[36] D.G.a.M. Goodwin, Harry K. and Speth, Raymond L., Cantera: An object-oriented software toolkit for chemical kinetics, thermodynamics, and transport processes, (2018).
[37] Day MS, Bell JB. Numerical simulation of laminar reacting flows with complexchemistry. Combust Theor Model 2000;4:535.
[38] Wang W, Egolfopoulos F. Preferential vaporization effects on the ignition of multi-component droplets. Proc Combust Inst 2024;40:105639.
[39] G.P. Smith, Y. Tao, H. Wang, Foundational fuel chemistry model version 1.0 (FFCM-1), epub, accessed July, 26 (2016) 2018.
[40] Ghahremani FA, Rubio M, Hauck C, Medchill C, Egolfopoulos FN, Cronin SB. In situ spectroscopic analysis and kinetic modeling of plasma-enhanced methane combustion. Fuel 2026;411:137885.
[41] Kawahara N, Hashimoto S, Tomita E. Spark discharge ignition process in a spark-ignition engine using a time series of spectra measurements. Proc Combust Inst 2017;36:3451–8.
[42] P.F. Bernath, Spectra of atoms and molecules, Oxford university press2025.
[43] Sheehe SL, Jackson SI. Identification of species from visible and near-infrared spectral emission of a nitromethane-air diffusion flame. J Mol Spectrosc 2019;364:111185.
[44] Gupta U, Vlachos DG. Reaction Network Viewer (ReNView): an open-source framework for reaction path visualization of chemical reaction systems. SoftwareX 2020;11:100442.